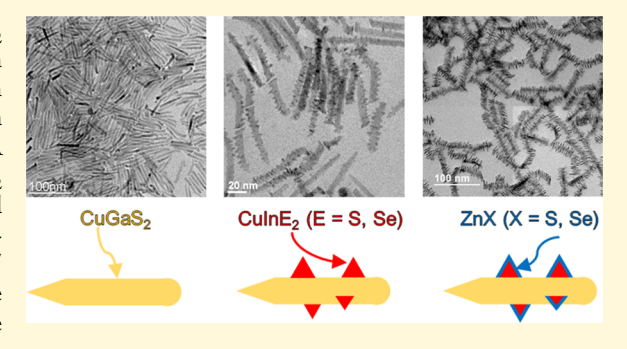
Downloaded by UNIV ILLINOIS URBANA-CHAMPAIGN at 21:41:41:204 on June 17, 2019 from https://pubs.acs.org/doi/10.1021/acs.chemmater.8b04769

# CuGaS<sub>2</sub>-CuInE<sub>2</sub> (E = S, Se) Colloidal Nanorod Heterostructures

Nuri Oh, †, § Logan P. Keating, ‡, § Gryphon A. Drake, ‡ and Moonsub Shim\*, ‡

Supporting Information

ABSTRACT: Colloidal nanorod heterostructures of I-III-VI semiconductors have been synthesized in a solution starting from wurtzite-like CuGaS2 nanorods. Growth of CuInS2 or CuInSe2 on CuGaS2 nanorods results in interesting sawtooth structures with larger lattice strain leading to sharper, more pronounced teeth. A final inorganic shell of ZnSe or ZnS grown on the CuGaS2/CuInSe2 nanorod heterostructures enhances photoluminescence. Unusual brush-like structures arise with prolonged ZnSe growth. Timeresolved photoluminescence measurements on CuGaS<sub>2</sub>/CuInSe<sub>2</sub>/ ZnS nanorod heterostructures reveal a lifetime approaching one microsecond, suggesting charge separation within the nanorods. The results shown here provide previously unknown nanorod hetero-



structures exhibiting interesting and potentially useful optical properties along with insights into heterostructure formation in colloidal I-III-VI2 nanorods.

# 1. INTRODUCTION

The combination of size/shape-tunable properties and solution processability of colloidal quantum dots (QDs) has generated considerable excitement in several areas including biomedical imaging, solid state lighting, and displays. Heterostructures of nanocrystals, from well-established core/shells to emerging anisotropic structures, can lead to new or improved capabilities and are often necessary for most applications. 4-7 A wide band gap shell with type I straddling band offset with the core material has been critical for essentially all applications exploiting photoluminescence (PL) of QDs. Reduced symmetry, e.g., as in nanorods (NRs), can provide additional advantages. Nanorod heterostructures (NRHs) with type II band offset have been shown to exhibit efficient photoinduced charge separation and directionality that are useful in photovoltaics and photocatalysis. <sup>12,13</sup> More recently, anisotropy and independent control over electron- and holeinjection processes demonstrated in double-heterojunction nanorods (DHNRs) have led not only to improvements in electroluminescence but also to simultaneous photodetection capabilities that can allow multifunctional optoelectronics and displays with new modes of interactivity.3,14-17 Anisotropic heterostructures of colloidal QDs can, in principle, be developed with a wide range of sizes, shapes, and compositions (and essentially unlimited combinations thereof) that may be useful for advancing many technologies. 18 However, the best performance achieved thus far has been in Cd-based II-VI materials that face severe usage restrictions in consumer products.<sup>19</sup> Hence, expanding the composition space for colloidal nanocrystal heterostructures of varying shapes should facilitate practical implementation. Furthermore, a broader

composition range should widen the achievable optical and electronic properties that can be tailored for a given application.

Colloidal nanocrystals of I-III-VI2 compound semiconductors have crystal structures similar to those of II-VI materials and much of the chemistry developed for II-VI nanocrystal heterostructures can and has been adapted, especially for CuInS<sub>2</sub> and CuInSe<sub>2</sub>. <sup>20-24</sup> An elegant approach to I-III-VI2 NRHs is via cation exchange of II-VI NRHs. For example, sequential cation exchange from CdSe/CdS dot-inrods to Cu<sub>2</sub>Se/Cu<sub>2</sub>S then to CuInSe<sub>2</sub>/CuInS<sub>2</sub> allows the initial morphology to be retained while eliminating the need to develop an entirely new synthetic route to I-III-VI2 NRs. 25 However, it may be difficult to achieve selectivity for different cations. For example, there is no obvious means of converting CdSe/CdS to CuInSe<sub>2</sub>/CuGaS<sub>2</sub>, since conditions that favor exchange of Cd in CdSe would also lead to exchange of Cd in CdS. Spatially varied cations in II-VI heterostructures may also be lost through cation exchange (e.g., cation exchange of CdSe/ZnS may lead to both Cd and Zn being exchanged to a common set of cations). Furthermore, a significant amount of impurities can be left over from cation exchange steps and can adversely alter the desired electronic/optical properties. Hence, direct synthesis of colloidal I-III-VI2 NRs and subsequent epitaxial growth of heterostructures is desirable.

Although chalcopyrite is the thermodynamically favored crystal structure, the wurtzite equivalent, which can facilitate

Received: November 15, 2018 Revised: February 25, 2019 Published: February 27, 2019

<sup>&</sup>lt;sup>†</sup>Division of Materials Science and Engineering, Hanyang University, Seoul 04763, Republic of Korea

 $<sup>^\</sup>ddagger$ Department of Materials Science and Engineering and Frederick Seitz Materials Research Laboratory, University of Illinois, Urbana, Illinois 61801, United States

directional NR growth, can also be achieved with I-III-VI2 semiconductors. Indeed, NRs of CuInS<sub>2</sub> and even their heterostructures have been achieved without employing cation exchange of II–VI materials. However, there have been only a limited number of reports, and the growth mechanisms are quite different, usually involving a combination of catalytic growth and cation exchange from Cu<sub>2-x</sub>S seeds.<sup>23-26,28</sup> Even less work has been carried out on CuGaS, NRs<sup>29,30,35-39</sup> and reports on growth of heterostructures from them are essentially nonexistent, with only one recent report. 30 Here, we examine and develop heterostructures starting from CuGaS2 NRs. Sawtooth-shaped CuGaS<sub>2</sub>/CuInS<sub>2</sub> and CuGaS<sub>2</sub>/CuInSe<sub>2</sub> NRHs are achieved with subtle variations in shape caused by differences in lattice mismatch. Additional growth of ZnS or ZnSe on CuGaS<sub>2</sub>/CuInSe<sub>2</sub> NRHs leads to the appearance of room-temperature PL from CuInSe2 with the extended growth of ZnSe resulting in interesting branched structures.

#### 2. EXPERIMENTAL SECTION

**2.1. Materials.** Trioctylphosphine oxide (TOPO) (90%), trioctylphosphine (TOP) (90%), oleic acid (OA) (90%), oleylamine (OAm) (70%), octadecene (ODE) (90%), CdO (99.5%), copper(I) acetate (CuOAc) (99.99%), gallium acetylacetonate (Ga(acac)<sub>3</sub>) (99.99%), In(III) acetate (In(OAc)<sub>3</sub>) (99.99%), zinc acetate (Zn(ac)<sub>2</sub>) (99.99%), 1-dodecanethiol (1-DDT) (>98%), sulfur (99.998%), and selenium (99.99%) were obtained from Sigma-Aldrich. Sodium oleate (Na-oleate) (>97%) was obtained from Tokyo Chemical Industry. N-Octadecylphosphonic acid (ODPA) (>99%) was obtained from PCI Synthesis. ACS grade chloroform and methanol were obtained from Fischer Scientific. All chemicals were used as received.

2.2. Synthesis of CuGaS2 Seed NRs. A flask was charged with CuOAc (24.5 mg, 0.2 mmol), Ga(acac)<sub>3</sub> (73.4 mg, 0.2 mmol), and 5 ml 1-DDT. The solution was stirred magnetically in a 25 mL threeneck round-bottom flask. The mixture was degassed under vacuum for 15 s, followed by an N2 or Ar purge. The solution was then heated to 240 °C at a rate of 30 °C/min. The yellow solution became clear and then changed to a deep yellow suspension. It was found that a slight excess of CuOAc would cause the solution to abruptly turn black once the 1-DDT thermolysis temperature was reached. This event was usually used as t = 0 for times when aliquots were taken out and other references to reaction time. The reaction was quenched by cooling to room temperature via an air jet. The final solution was suspended in a 1:2 mixture of chloroform/ethanol and centrifuged at 2000 rpm. The precipitate was resuspended in chloroform for the next step. Aliquots for high-resolution transmission electron microscope (HRTEM) analysis were prepared by washing the crude reaction mixture with the 1:2 chloroform/ethanol solution three times, resuspending in chloroform, and drop-casting onto transmission electron microscope (TEM) grids. The grids were then held under vacuum for 24 h at 100 °C prior to imaging.

2.3. Synthesis of CuGaS<sub>2</sub>/CuInS<sub>2</sub> NRHs. A mixture of In(OAc)<sub>3</sub> (58.4 mg, 0.2 mmol) and OA (0.19 mL, 0.6 mmol) in 3 mL of ODE was added to a 25 mL three-neck round-bottom flask and degassed at 120 °C for 30 min under vacuum. The solution was then heated to 250 °C under N<sub>2</sub> or Ar atmosphere to form In-oleate. After 1 h, the In-oleate solution was cooled to 60 °C. A purified solution of CuGaS<sub>2</sub> NR seeds (half of the purified reaction mixture from Section 2.2) was injected into the solution and the chloroform was allowed to evaporate for 30 min under vacuum. After heating to 250 °C under inert atmosphere, 1 ml of 0.2 M ODE-S solution (0.2 mmol S) was slowly injected at a rate of 8 mL/h (7.5 min total injection time) and the reaction mixture was allowed to stir at 180 °C for 5 min prior to cooling to room temperature by an air jet. The crude product was flocculated using a mixture of acetone, toluene, and ethanol and centrifuged at 2000 rpm until a pellet was formed. The supernatant was removed, and the pellet was re-flocculated using the same mixture of solvents. After centrifuging, and decanting the supernatant, the

pellet was redissolved using chloroform and prepared as a solution for the next step.

2.4. Synthesis of CuGaS<sub>2</sub>/CuInSe<sub>2</sub> NRHs. A mixture of In(OAc)<sub>3</sub> (58.4 mg, 0.2 mmol) and OA (0.19 mL, 0.6 mmol) in 5 mL of ODE was added to a 25 mL 3-neck round-bottom flask and degassed at 100 °C for 30 min under vacuum. The reaction mixture was then heated to 250 °C and held there for 1 h to form In-oleate. Following this, the reaction mixture was cooled to 60 °C and a solution of purified CuGaS2 NRs in chloroform (half of the reaction product from Section 2.2) was injected. The chloroform was then removed by vacuum and the solution was reheated to 260 °C under inert atmosphere. While at 260 °C, 0.8 mL of 0.25 M TOPSe solution was slowly added at a rate of 8 mL/h (6 min total injection time). Once the injection was finished, the reaction mixture was cooled to room temperature by an air jet. The crude product was flocculated using a mixture of acetone, toluene, and ethanol and centrifuged at 2000 rpm until a pellet was formed. The supernatant was removed, and the pellet was re-flocculated using the same mixture of solvents. After centrifuging and decanting the supernatant, the pellet was redissolved using chloroform and prepared as a solution for the next

2.5. Synthesis of CuGaS<sub>2</sub>/CuInSe<sub>2</sub>/ZnS DHNRs. A mixture of Zn(OAc)<sub>2</sub> (91.7 mg, 0.5 mmol) and oleic acid (0.32 mL, 1.0 mmol) in 3 mL of ODE was added to a 25 mL three-neck round-bottom flask and degassed at 120 °C for 30 min under vacuum. The solution was then heated to 250 °C under N<sub>2</sub> or Ar atmosphere to form Zn-oleate. After 1 h, the Zn-oleate solution was cooled to 60 °C. A purified solution of CuGaS<sub>2</sub>/CuInSe<sub>2</sub> NRH seeds (the entire purified reaction mixture from Section 2.4) was injected into the solution and the chloroform was evaporated for 30 min under vacuum. Then, a solution of 3 mL of 1-DDT, 1 mL of TOP, and 0.5 mL of OAm was injected into the reaction flask under inert atmosphere. After heating to 250 °C, the reaction mixture was stirred for 10 h prior to cooling to room temperature. The crude product was flocculated using a mixture of acetone, toluene, and ethanol and centrifuged at 2000 rpm until a pellet was formed. The supernatant was removed and the pellet was re-flocculated using the same mixture of solvents. The pellet was then resuspended using chloroform for TEM or optical measurement.

2.6. Synthesis of CuGaS<sub>2</sub>/CuInSe<sub>2</sub>/ZnSe DHNRs. A mixture of Zn(OAc)<sub>2</sub> (91.7 mg, 0.5 mmol) and OA (0.32 mL, 1.0 mmol) in 3 mL of ODE was added to a 25 mL three-neck round-bottom flask and degassed at 120 °C for 30 min under vacuum. The solution was then heated to 250 °C under N2 or Ar atmosphere to form Zn-oleate. After 1 h, the Zn-oleate solution was cooled to 60 °C. A purified solution of CuGaS<sub>2</sub>/CuInSe<sub>2</sub> NRH seeds (the entire purified reaction mixture from Section 2.4) was injected into the solution and the chloroform was allowed to evaporate for 30 min under vacuum. After heating to 250 °C under inert atmosphere, 1 mL of 0.25 M TOPSe solution (20 mg Se, 0.25 mmol in 1 mL TOP) was slowly injected at 250 °C at a rate of 4 mL/h (15 min total injection time). At the conclusion of the injection, the reaction mixture was allowed to stir at 250 °C for 5 min prior to cooling to room temperature by an air jet. The crude product was flocculated using a mixture of acetone, toluene, and ethanol and centrifuged at 2000 rpm until a pellet was formed. The supernatant was removed and the pellet was re-flocculated using the same mixture of solvents. The pellet was then resuspended using chloroform for TEM or optical measurement.

**2.7. Characterization.** TEM samples were prepared on Au or Cu grids with a thin carbon film from a dilute solution of nanocrystals in chloroform. TEM analysis was carried out with a JEOL 2100 TEM or JEOL 2011 TEM, both operating at 200 kV. Energy-dispersive X-ray spectroscopy (EDX) and scanning transmission electron microscope (STEM) analyses were carried out with a JEOL JEM-2200FS aberration-corrected STEM/TEM operating at 200 kV. UV—vis absorption spectra were obtained with an Agilent 8453 photodiode array spectrometer. Powder X-ray diffraction (PXRD) samples were prepared by drop-casting purified NRs in chloroform onto a glass microscope slide. PXRD spectra were obtained using a Rigaku MiniFlex 600. PL spectra were collected with a Horiba Jobin Yvon FluoroMax-3 spectrofluorometer. PL lifetime measurements were

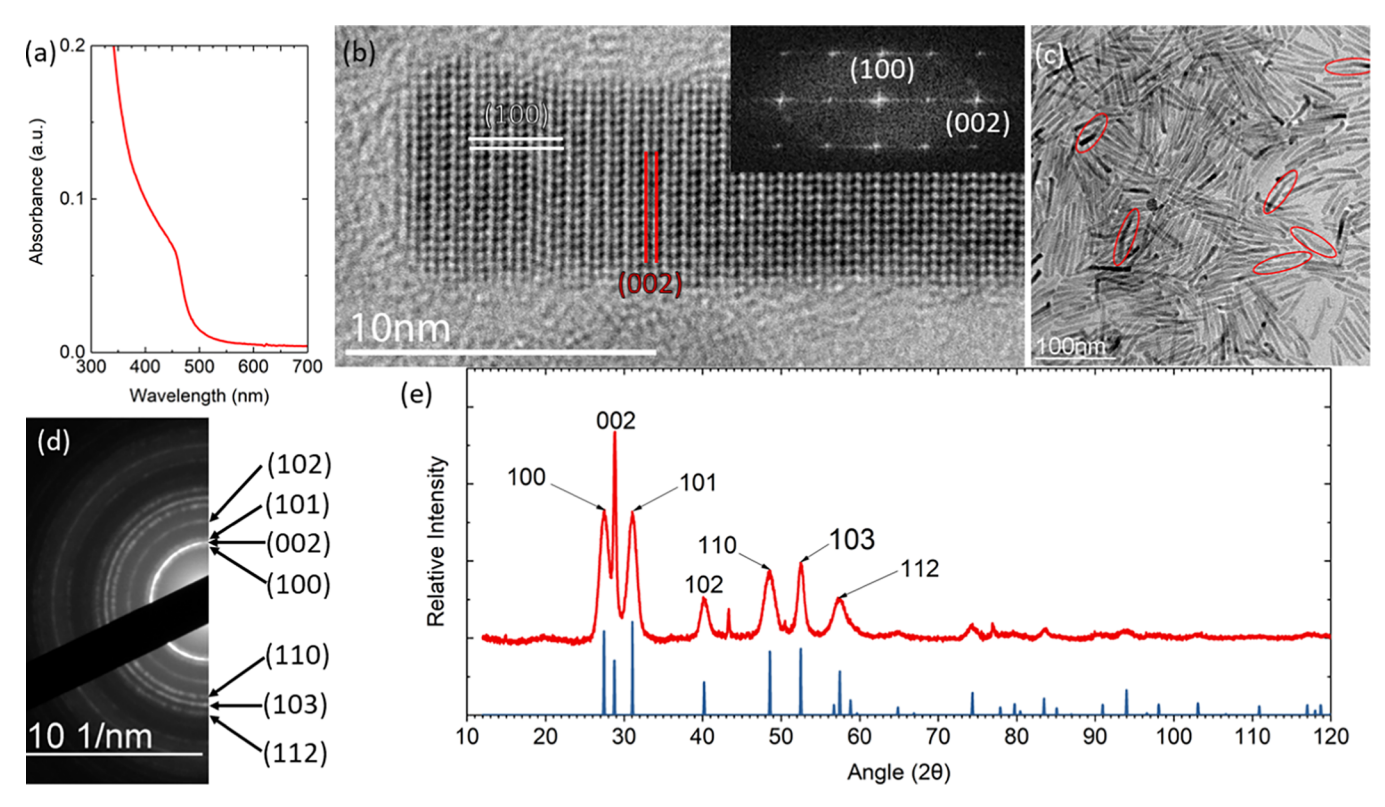


Figure 1. (a) UV-vis spectrum of CuGaS<sub>2</sub> NRs suspended in toluene, which shows an absorption shoulder around 460 nm (~2.7 eV). (b) HRTEM of a CuGaS<sub>2</sub> NR along with inset FFT. The FFT indicates that the rod is composed of a wurtzite-like phase, though we note the presence of several stacking faults near the tip of the rod. (c) Low-magnification TEM of CuGaS<sub>2</sub> NRs showing consistent rod growth. Red ovals indicate rods that exhibit the characteristic "bent" morphology. (d) Selected area electron diffraction (SAED) of CuGaS<sub>2</sub> NRs, which indicates the presence of a wurtzite-like phase. (e) PXRD of CuGaS<sub>2</sub> NRs, along with a simulated pattern for bulk wurtzite-like CuGaS<sub>2</sub>. The simulated and experimental patterns are in excellent agreement excluding the peak at ~43°.

collected with a Horiba Jobin Yvon Nanolog with a 400 nm pulsed laser excitation source.

#### 3. RESULTS AND DISCUSSION

**3.1. CuGaS<sub>2</sub> Nanorods.** CuGaS<sub>2</sub> NRs were synthesized by a heat-up method with CuOAc and Ga(acac)<sub>3</sub> in 1-DDT, which was modified from a previously reported method.<sup>35</sup> The main difference from the prior method was that 1-DDT was used as both ligand and solvent instead of a mixture of ODE and 1-DDT. Figure 1a shows the UV-vis spectrum of the CuGaS<sub>2</sub> NRs. The absorption shoulder observed near 460 nm is at a higher energy than the expected band gap for bulk CuGaS<sub>2</sub>, suggesting quantum confinement. High- and lowresolution TEM images of the NRs are shown in Figure 1b,c. Nanorods taper toward one end and have an average diameter of ~5 nm, with an average length of ~53 nm. The fast Fourier transform (FFT) in the inset of Figure 1b reveals that the NR has a wurtzite-like crystal structure. Larger area electron diffraction and PXRD shown in Figure 1d,e indicate that the wurtzite-like structure is predominant for these CuGaS<sub>2</sub> NRs.

The wurtzite structure is either energetically more favorable than the zinc blende structure or more easily accessible at nanometer dimensions for Cd-based II—VI nanocrystals, which can facilitate anisotropic growth given proper ligands that can differentiate growth rates along different crystallographic directions. The zinc blende-based chalcopyrite structure, on the other hand, is significantly favored energetically over the wurtzite equivalent phase for Cu-based I—III—VI<sub>2</sub>, sulfides. A previous study of CuGaS<sub>2</sub> nanocrystals determined that the energy difference between chalcopyrite and wurtzite-like

phases was approximately 0.38 eV/formula unit.35 However, I-III-VI2 sulfide nanocrystals, especially NRs and other anisotropic shapes, often grow from copper sulfide (Cu<sub>2-r</sub>S) seeds with hexagonal chalcocite and/or monoclinic djurleite phases.<sup>43</sup> The anions in Cu<sub>2-x</sub>S maintain a wurtzite-like scaffold, and NRs of I-III-VI<sub>2</sub> semiconductors can be achieved through a combination of cation exchange and catalytic growth. This mechanism is now well-established for CuInS<sub>2</sub> NR growth.<sup>23</sup> In our synthesis of CuGaS<sub>2</sub> NRs, Cu<sub>2-x</sub>S nanocrystals first form at or around 240 °C, followed by the nucleation of CuGaS2 on one side of Cu2-xS nanocrystals, which subsequently leads to CuGaS2 NR growth, presumably through a combination of catalytic growth and cation exchange similar to CuInS<sub>2</sub> NR growth. <sup>29,30,32</sup> We suspect that the tapering seen in essentially all NRs arises from this combination of catalytic growth and cation exchange, where the catalytic Cu<sub>2-x</sub>S particles continuously become smaller due to cation exchange until they are completely converted to CuGaS<sub>2</sub>. A similar tapering observed in Cu<sub>2-x</sub>S/ZnS NRHs has been attributed to this mechanism. Tapering is also sometimes seen in CuInS2 NRs, and the same mechanism may be involved.<sup>26,32</sup>

Interestingly, and unlike most CuInS<sub>2</sub> NRs reported, approximately 10% of the CuGaS<sub>2</sub> NRs grown exhibit a bent morphology, where the growth direction appears to change during the course of the reaction. Preliminary studies indicate that it is unlikely that the bend arises from a change in crystal structure. Supporting Information Figure S1 shows a high-resolution TEM (HRTEM) of a bent nanorod, which is wurtzite throughout the bent region. PXRD in Figure 1e shows

the dominance of a wurtzite-like phase, which matches the simulated diffraction pattern for bulk wurtzite CuGaS<sub>2</sub>. The high-resolution TEM studies, as exemplified by Figure 1b, indicate that nearly all rods are completely wurtzite, with only occasional stacking faults, which are mostly near the tips rather than at the bends. Further studies exploring this interesting observation are underway.

3.2. CuGaS<sub>2</sub>/CuInSe<sub>2</sub> and CuGaS<sub>2</sub>/CuInS<sub>2</sub> NRHs. As the next step toward I-III-VI2-based NR heterostructures, we have attempted to grow CuInS2 or CuInSe2 on CuGaS2 NRs. In ternary I–III–VI<sub>2</sub> compound nanocrystals, it is well-known that the cation precursors for the secondary component can alter the composition by interdiffusion/substitution of cations in the lattice of the pre-existing seed nanocrystals. 25,43,44 A key challenge here is the inhibition of this undesirable cation diffusion by the selection of proper precursors or other reaction conditions. Our efforts to address this issue include selecting ligands with poor Cu affinity to inhibit/minimize loss of Cu from CuGaS<sub>2</sub> seed nanorods and ensuring careful purification to remove unreacted Cu2-x nanoparticles. Presynthesized CuGaS2 NRs were purified and transferred to the In-oleate/ODE solution. Slow addition of TOPSe at an elevated temperature led to the color of reaction mixture changing from yellow to reddish brown. Figure 2a shows the corresponding change in the absorption spectrum. The increase of the absorption tail in the 500-700 nm region indicates that a secondary component having a smaller band gap grows with increasing amount of Se precursor. Surprisingly, the introduction of In-oleate and TOPSe at 260 °C leads to the growth of sawtooth-like structures on the sides of CuGaS<sub>2</sub> NRs, as shown in Figure 2b,c. The FFT and HRTEM images in Figure 2c reveal that the lattice constant of the secondary component is larger than that of CuGaS2. Based on the combination of elements used, the possible compositions of the secondary component are CuGaS2

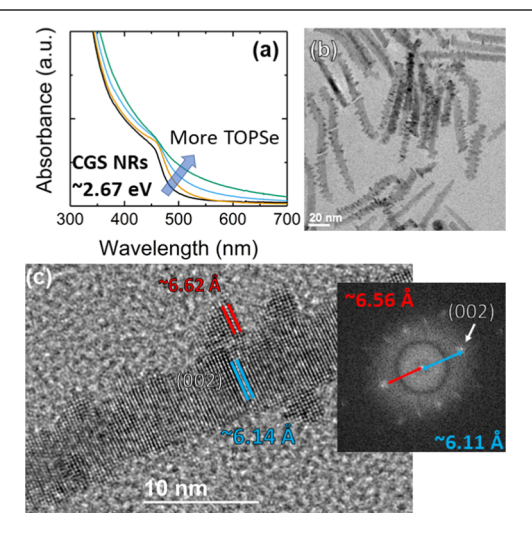


**Figure 2.** Absorption spectra and TEM images of CuGaS<sub>2</sub>/CuInSe<sub>2</sub> NRHs. (a) Absorption spectra during the growth of the secondary component. As more TOPSe is injected, the absorption tails become more pronounced in the region from 500 to 700 nm, indicating CuInSe<sub>2</sub> growth. (b) Low-magnification TEM image after TOPSe addition, showing pronounced sawtooth-like structures. (c) HRTEM of a NRH. Inset is the FFT of the rod showing multiple (002) reflections. Measured lattice fringes indicate a composition difference between the body of the rod and the "teeth".

(wurtzite-like lattice parameter c = 6.188 Å), <sup>45</sup> CuGaSe<sub>2</sub> (6.434 Å), <sup>46</sup> CuInS<sub>2</sub> (6.425 Å), <sup>45</sup> CuInSe<sub>2</sub> (6.727 Å), <sup>47</sup> or their alloys. The lattice spacing shown in Figure 2c and the PXRD (Figure S2) best correspond to CuInSe2, which has the largest lattice constant among the candidates. Some of the smaller lattice constants observed may arise from strain due to lattice mismatch with CuGaS2 and/or alloying near the interface. We note that the second largest lattice constant material, CuInS2, is still smaller than the smallest measured lattice spacing. It is also interesting to note that as the size of the side-growth decreases, the observed lattice spacing also decreases, which is consistent with the lattice mismatch due to distortion being more pronounced for smaller particles. Measurement of the lattice parameter of the sawtooth structures as a function of distance from the body of the NR indicates that the sawtooth structures have a continuously increasing lattice constant until the lattice parameter of CuInSe<sub>2</sub> is reached. This may explain the variation in measured lattice parameter for the smaller sawtooth structures. A fixed amount of alloying near the heterointerface leading to a larger volume fraction being alloyed for smaller particles could also explain this apparent trend.

High-resolution aberration-corrected STEM analysis was also carried out to verify the composition of the sawtooth NRHS (Figure 3). A full-length image of an individual NRH in Figure 3a indicates that each protruding tooth from the CuGaS<sub>2</sub> NR has a higher Z-contrast, and therefore consists of one or more heavier elements than the main rod. Atomic column intensity analysis from STEM images similar to Figure 3b,c reveals that the intensities of the cation columns in the side protrusions are slightly brighter than those of the cation columns in the seed NR. Although the nature of mixed elements in the cation sites of I-III-VI2 compound semiconductors makes composition analysis somewhat difficult, the higher intensity in the side protrusions is consistent with the inclusion of In. More clearly, the intensity of anion columns diminishes from the side protrusion to the center of the rod, confirming that the anions in the teeth are heavier than those of the main body of the rod, i.e., Se in the teeth and S in the main body of the rod. Energy-dispersive X-ray

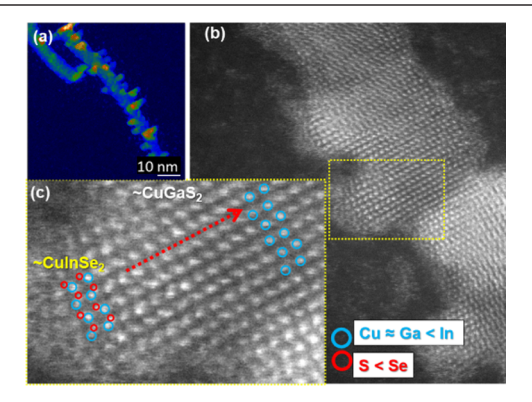


**Figure 3.** Z-contrast STEM of a CuGaS<sub>2</sub>/CuInSe<sub>2</sub> NRH. (a) False-color STEM image of a NRH showing higher Z-contrast in the grown protrusions than the main body of the rod. (b) High-resolution of NRH in (a). (c) Detail of the boxed region in (b). The anion columns in the side protrusion show higher Z-contrast, which is highlighted by the red circles. Tracking the Z-contrast of the anion columns moving toward the center of the rod, there is a reduction in Z-contrast intensity, consistent with a transition from CuInSe<sub>2</sub> to CuGaS<sub>2</sub>.

spectroscopy (EDX) elemental maps shown in Supporting Information Figure S3 further support this composition distribution with Ga and S evenly spread throughout the center part of the NRs and In and Se concentrated in the side protrusions. Therefore, we conclude that CuInSe<sub>2</sub> grows on the side of CuGaS<sub>2</sub> NRs.

We have also grown heterostructures using CuInS<sub>2</sub>, where In is the only new element added to the existing CuGaS<sub>2</sub> NRs. The introduction of In-oleate and ODE-S to CuGaS2 NR solution at 250 °C led to similar sawtooth-like structures on the surface of CuGaS<sub>2</sub> NRs as shown in the absorption spectra and TEM images in Figure 4. The UV-vis spectral evolution during growth shown in Figure 4a is similar to that of CuInSe<sub>2</sub> growth (Figure 2a), with the exception of the absorption tail not extending as far into the near-IR. The TEM image in Figure 4b reveals similar but less pronounced sawtooth-like growth on the sides of the CuGaS2 NRs. The high-resolution TEM image and the FFT in Figure 4c,d reveal that the lattice constant of the secondary component is slightly larger than that of CuGaS2 but much smaller than that of CuInSe2. The lattice parameter of the second phase is 6.40 Å, which is close to CuInS2. The lattice mismatch of CuGaS2 with CuInS2 is smaller than that with CuInSe2, allowing larger interfacial area due to reduced strain. This reduced strain effect is evident in the morphology of the heterostructures, with wider, and less peaked structures growing compared to the prominent sawtooth structures of CuInSe<sub>2</sub> on CuGaS<sub>2</sub>.

The growth of CuInSe<sub>2</sub> and CuInS<sub>2</sub> side protrusions described above is somewhat surprising in that only In and Se or S precursors were added to purified CuGaS<sub>2</sub> NRs. However, as previously shown, <sup>48</sup> metal oleates can etch II—VI NRs/nanocrystals, and a similar effect may be taking place here, i.e., In-oleate partially etches CuGaS<sub>2</sub> NRs, providing the required Cu precursor to grow CuInSe<sub>2</sub> or CuInS<sub>2</sub> upon Se or S precursor addition, respectively. Control experiments (Figure S4) do verify that CuGaS<sub>2</sub> NRs get etched and eventually begin to dissolve away upon extended heating in In-oleate solution.

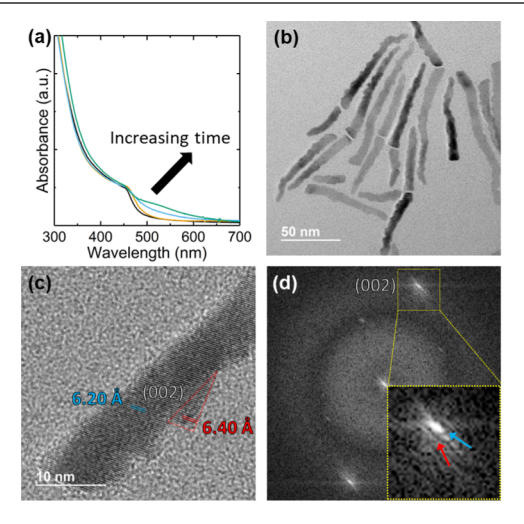


**Figure 4.** CuInS<sub>2</sub> growth on CuGaS<sub>2</sub> NRs using ODE-S and In-oleate. (a) Absorption spectrum during ODE injection in In-oleate solution. (b) Low-magnification image of CuGaS<sub>2</sub>/CuInS<sub>2</sub> NRHs showing the growth of smaller sawtooth-like structures. (c) HRTEM of NRHs, with the measured difference in lattice parameters highlighted. (d) FFT of (c) showing the presence of two lattice parameters.

3.3. ZnS and ZnSe Shell Growth on CuGaS<sub>2</sub>/CuInSe<sub>2</sub> NRHs. Although CuGaS<sub>2</sub>/CuInSe<sub>2</sub> and CuGaS<sub>2</sub>/CuInS<sub>2</sub> NRHs have interesting morphologies with subtle variations due to a different degree of lattice mismatch, they do not exhibit measurable room-temperature PL as synthesized. As a possible route to improved PL, we have attempted to grow an inorganic shell on CuGaS<sub>2</sub>/CuInSe<sub>2</sub> NRHs using Zn-oleate and S or Se precursors. First, ZnS shell growth was carried out with Zn-oleate and 1-DDT to determine if PL could be enhanced/observed. The TEM images and SAED shown in Figure 5a-d exhibit no obvious change to the overall shape and lattice spacings of the NRHs upon growing a ZnS shell. There is also no obvious change to the UV-vis absorption spectrum (Figure 5e). Nevertheless, there is a significant enhancement in PL intensity after introducing Zn and S precursors, indicating successful ZnS shell growth (Figure 5e). The absorption shoulder at ~450 nm corresponding to the band gap of the CuGaS<sub>2</sub> NRs is accompanied by an absorption tail extending out into the red. The PL at ~700 nm arising from CuInSe<sub>2</sub> exhibits a large pseudo-Stokes shift relative to the prominent absorption shoulder at ~450 nm corresponding to the band gap of the CuGaS2 NRs. The PL peak also blueshifts with reaction time. The direct growth of a ZnS shell can cause spectral shifts due to compressive strain and extension of the wave function out into the shell, but these effects are expected to lead to a red shift.<sup>49</sup> The blue shift and the enhancement of PL may then be arising from two possible scenarios: (1) Zn ions are incorporated into the NRHs, causing partial alloying 44 or partial cation exchange near the surface, and (2) Zn-oleate partially etches the CuInSe<sub>2</sub> before ZnS growth. 50 In both cases, the band gap increases due to

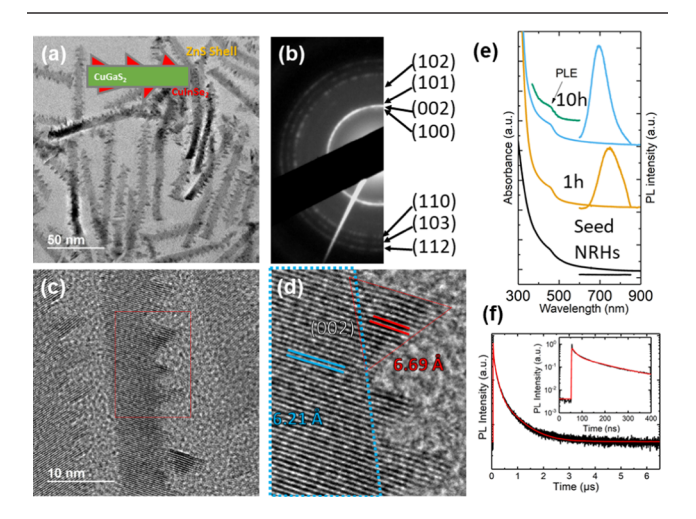


**Figure 5.** ZnS Shell growth on CuGaS<sub>2</sub>/CuInSe<sub>2</sub> NRHs with Znoleate and 1-DDT at 250 °C. (a) Low-magnification TEM image of CuGaS<sub>2</sub>/CuInS<sub>2</sub>/ZnS NRHs. (b) SAED pattern of the NRHs after growing a ZnS shell. (c, d) Low- and high-magnification images of CuGaS<sub>2</sub>/CuInSe<sub>2</sub>/ZnS NRHs. The average lattice parameter of the pyramid-shaped structure is 6.69 Å, and the center of the rod is 6.21 Å, which corresponds to CuInSe<sub>2</sub> and CuGaS<sub>2</sub> respectively. (e) Absorption and emission spectra before and after ZnS growth on the NRHs. The bottom spectrum is the seed CuGaS<sub>2</sub>/CuInSe<sub>2</sub> NRHs. PL excitation (PLE) spectrum is also shown for the final product. As the growth time increases from 1 to 10 h in the presence of Zn-oleate and ODE-S, the PL peak is blue-shifted and increases in intensity. (f) Time-resolved PL measurement along with three-exponential curve fitting. Time constants obtained from the curve fitting are  $τ_1$  = 16.2 ns (10.25%),  $τ_2$  = 126 ns (49.26%), and  $τ_3$  = 604 ns (40.48%).

effectively smaller size CuInSe<sub>2</sub>. In reality, the PL enhancement and blue shift are likely due to some combination of both mechanisms, with alloying likely being dominant. If etching prior to ZnS shell growth was dominant, one would anticipate a blue shift, followed by a red shift.

To better understand their optical characteristics, PL excitation (PLE) spectra and time-resolved PL of CuGaS<sub>2</sub>/ CuInSe<sub>2</sub>/ZnS NRHs were collected. The PLE spectrum (top spectrum of Figure 5e) is essentially identical to the absorption spectrum, which supports the formation of epitaxial CuGaS<sub>2</sub>/ CuInSe<sub>2</sub>/ZnS NRHs, i.e., radiative recombination occurs in CuInSe<sub>2</sub> even when photons are absorbed in the CuGaS<sub>2</sub> component. Time-resolved PL measurements show multiexponential decay (Figure 5f). Three-exponential fit leads to around 10% of the 16 ns component, 50% of the 126 ns component, and 41% of the 600 ns component. The highest fractional intensity component shows a ~100-200 ns time constant, similar to values reported for "spherical" I-III-VI2 nanocrystals. 51,52 It is notable that these NRHs exhibit an extremely long PL lifetime of 600 ns, with nearly equivalent fractional intensity. Although we cannot completely rule out surface-trap-mediated emission as a possible origin of this long lifetime, given that the typical full width at half-maximum of such emissions are >~200 nm for many semiconductor nanocrystals, the observed linewidth of ~100 nm may be more consistent with radiative recombination from a charge separated state within the NRH.<sup>53</sup> We expect the band alignment to be quasi-type-II, with CuGaS<sub>2</sub> and CuInSe<sub>2</sub> sharing a similar valence band edge position. Given this band alignment, it is likely that the hole may be delocalized upon photoexcitation, with significant density in the CuGaS<sub>2</sub> NR. Consequently, the hole can then fall into a Cu-ion-based intragap state in the CuGaS2, whereas the electron is localized in one of the CuInSe<sub>2</sub> particles.<sup>54</sup> This would result in a charge-separated state within the nanoparticle. Charge separation within a particles is known to cause long PL lifetime.5

Finally, we have attempted to grow ZnSe on CuGaS<sub>2</sub>/ CuInSe2 NRHs as an alternate means of enhancing PL while achieving a band alignment similar to a double heterojunction. Purified CuGaS<sub>2</sub>/CuInSe<sub>2</sub> NRHs were injected into Zn-oleate solution followed by slow addition of TOPSe (see Experimental Section details). Figure 6a shows the appearance of a PL peak around 720 nm following the growth of a ZnSe shell (TEM image in Figure 6b). This peak position is slightly more red-shifted from the ZnS shell, presumably due to the smaller band offset of ZnSe with CuInSe2. This could cause more spreading of the electron wave function from the core to the shell, resulting in a red-shifted PL. When the growth of a thick ZnSe shell was attempted, the growth of long side protrusions on the CuInSe<sub>2</sub> structures was observed (Figure 6c,d). Compared to Figure 6b, there is an obvious elongation of the secondary component with increasing reaction time. The lattice mismatch between CuInSe<sub>2</sub> and ZnSe is only 2%, which may favor selective heteroepitaxy compared to the body of the CuGaS2 NR.

# 4. CONCLUSIONS

We have successfully synthesized CuGaS<sub>2</sub>-based colloidal NRHs with some unusual morphologies. The starting CuGaS<sub>2</sub> seed NRs taper at one end and have a wurtzite-like phase throughout. Epitaxial growth of CuInS<sub>2</sub> or CuInSe<sub>2</sub> leads to sawtooth-shaped NRHs, with larger lattice mismatch

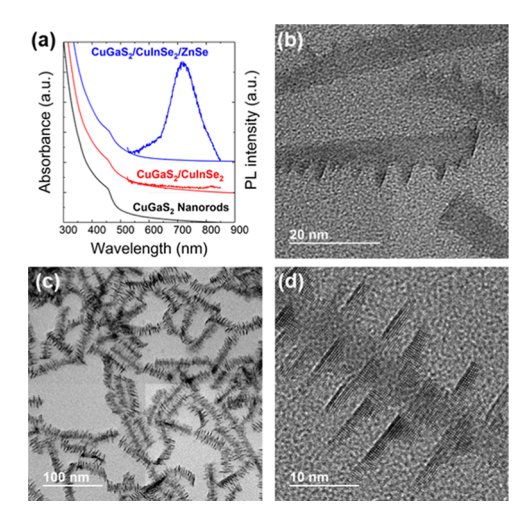


**Figure 6.** CuGaS $_2$ /CuInSe $_2$ /ZnSe double-heterojunction NRs (DHNRs). (a) Absorption and emission spectra of CuGaS $_2$  NRs, CuGaS $_2$ /CuInSe $_2$  NRHs, and CuGaS $_2$ /CuInSe $_2$ /ZnSe DHNRs. (b) Low-magnification TEM image of CuGaS $_2$ /CuInSe $_2$ /ZnSe DHNRs. (c, d) Low- and high-magnification TEM images of branched structures formed by extended reaction conditions. Measurements of the lattice spacing in the side branches are consistent with ZnSe lattice parameters.

causing sharper, more pronounced teeth that have smaller interfacial area. Growth of ZnS shell on  $CuGaS_2/CuInSe_2$  NRHs leads to enhanced PL and other interesting/useful optical properties, including large pseudo-Stokes shift and charge separation within the NRH. Changing the final shell composition to ZnSe leads to similar features as those of ZnS shell initially, but continued growth results in unusual brush-like structures.

#### ASSOCIATED CONTENT

# **S** Supporting Information

The Supporting Information is available free of charge on the ACS Publications website at DOI: 10.1021/acs.chemmater.8b04769.

EDX maps, along with additional TEM of NRs and STEM of NRHs; bent CuGaS<sub>2</sub> nanorod (Figure S1); PXRD of a dropcast film of CuGaS<sub>2</sub>/CuInSe<sub>2</sub> NRHs (Figure S2); EDX Mapping of a CuGaS<sub>2</sub>/CuInSe<sub>2</sub> nanorod (Figure S3); TEM of In-oleate etching experiment (Figure S4) (PDF)

## AUTHOR INFORMATION

## **Corresponding Author**

\*E-mail: mshim@illinois.edu.

ORCID

Nuri Oh: 0000-0001-9145-8911

Logan P. Keating: 0000-0002-1106-9658 Moonsub Shim: 0000-0001-7781-1029

## **Author Contributions**

§N.O. and L.P.K. contributed equally to this work.

## **Author Contributions**

All authors have given approval to the final version of the manuscript.

## **Funding**

This work was supported by the NSF (Grant 1825356).

#### Notes

The authors declare no competing financial interest.

## ACKNOWLEDGMENTS

Experiments were carried out in part in the Frederick Seitz Materials Research Laboratory Central Facilities at University of Illinois.

## ABBREVIATIONS

QDs, quantum dots; PL, photoluminescence; NRs, nanorods; NRHs, nanorod heterostructures; DHNRS, double-heterojunction nanorods; TOPO, trioctylphosphine oxide; TOP, trioctylphosphine; OA, oleic acid; OAm, oleylamine; ODE, octadecene; 1-DDT, 1-dodecanethiol; ODPA, octadecylphosphonic acid; TEM, transmission electron microscope; PXRD, powder X-ray diffraction; STEM, scanning transmission electron microscope; FFT, fast Fourier transform; SAED, selected area electron diffraction; HRTEM, high-resolution transmission electron microscope; EDX, energy-dispersive X-ray spectroscopy; PLE, photoluminescence excitation

#### REFERENCES

- (1) Wegner, K. D.; Hildebrandt, N. Quantum Dots: Bright and Versatile in Vitro and in Vivo Fluorescence Imaging Biosensors. *Chem. Soc. Rev.* **2015**, *44*, 4792–4834.
- (2) Jun, S.; Lee, J.; Jang, E. Highly Luminescent and Photostable Quantum Dot-silica Monolith and Its Application to Light-Emitting Diodes. *ACS Nano* **2013**, *7*, 1472–1477.
- (3) Nam, S.; Oh, N.; Zhai, Y.; Shim, M. High Efficiency and Optical Anisotropy in Double-Heterojunction Nanorod Light-Emitting Diodes. ACS Nano 2015, 9, 878–885.
- (4) Bang, J.; Park, J.; Lee, J. H.; Won, N.; Nam, J.; Lim, J.; Chang, B. Y.; Lee, H. J.; Chon, B.; Shin, J.; et al. ZnTe/ZnSe (Core/Shell) Type-II Quantum Dots: Their Optical and Photovoltaic Properties. *Chem. Mater.* **2010**, 22, 233–240.
- (5) Kim, S.; Fisher, B.; Eisler, H. J.; Bawendi, M. Type-II Quantum Dots: CdTe/CdSe(Core/Shell) and CdSe/ZnTe(Core/Shell) Heterostructures. *J. Am. Chem. Soc.* **2003**, *125*, 11466–11467.
- (6) McDaniel, H.; Heil, P. E.; Tsai, C.-L.; Kim, K.; Shim, M. Integration of Type II Nanorod Heterostructures into Photovoltaics. *ACS Nano* **2011**, *5*, 7677–7683.
- (7) Lee, S.; Flanagan, J. C.; Kang, J.; Kim, J.; Shim, M.; Park, B. Integration of CdSe/CdSe<sub>x</sub>Te<sub>1-x</sub> Type-II Heterojunction Nanorods into Hierarchically Porous TiO2 Electrode for Efficient Solar Energy Conversion. *Sci. Rep.* **2015**, *5*, No. 17472.
- (8) Hines, M. A.; Guyot-Sionnest, P. Synthesis and Characterization of Strongly Luminescing ZnS-Capped CdSe Nanocrystals. *J. Phys. Chem.* **1996**, *100*, 468–471.
- (9) Danek, M.; Jensen, K. F.; Murray, C. B.; Bawendi, M. G. Synthesis of Luminescent Thin-Film CdSe/ZnSe Quantum Dot Composites Using CdSe Quantum Dots Passivated with an Overlayer of ZnSe. *Chem. Mater.* **1996**, *8*, 173–180.
- (10) Rodriguez-Viejo, J.; Jensen, K. F.; Mattoussi, H.; Michel, J.; Dabbousi, B. O.; Bawendi, M. G. Cathodoluminescence and Photoluminescence of Highly Luminescent CdSe/ZnS Quantum Dot Composites. *Appl. Phys. Lett.* **1997**, *70*, 2132–2134.
- (11) Schlamp, M. C.; Peng, X.; Alivisatos, A. P. Improved Efficiencies in Light Emitting Diodes Made with CdSe(CdS) Core/Shell Type Nanocrystals and a Semiconducting Polymer. *J. Appl. Phys.* **1997**, *82*, 5837–5842.
- (12) Shim, M.; Mcdaniel, H.; Oh, N. Prospects for Strained Type-II Nanorod Heterostructures. J. Phys. Chem. Lett. 2011, 2, 2722–2727.
- (13) Shim, M.; McDaniel, H. Anisotropic Nanocrystal Heterostructures: Synthesis and Lattice Strain. *Curr. Opin. Solid State Mater. Sci.* **2010**, *14*, 83–94.

- (14) Oh, N.; Nam, S.; Zhai, Y.; Deshpande, K.; Trefonas, P.; Shim, M. Double-Heterojunction Nanorods. *Nat. Commun.* **2014**, *5*, No. 3642.
- (15) Jiang, Y.; Oh, N.; Shim, M. Double-Heterojunction Nanorod Light-Emitting Diodes with High Efficiencies at High Brightness Using Self-Assembled Monolayers. *ACS Photonics* **2016**, *3*, 1862–1868
- (16) Oh, N.; Kim, B. H.; Cho, S.-Y.; Nam, S.; Rogers, S. P.; Jiang, Y.; Flanagan, J. C.; Zhai, Y.; Kim, J.-H.; Lee, J.; et al. Double-Heterojunction Nanorod Light-Responsive LEDs for Display Applications. *Science* **2017**, *355*, *616*–*619*.
- (17) Cho, S.-Y.; Oh, N.; Nam, S.; Jiang, Y.; Shim, M. Enhanced Device Lifetime of Double-Heterojunction Nanorod Light-Emitting Diodes. *Nanoscale* **2017**, *9*, 6103–6110.
- (18) Hu, J.; Li, L.; Yang, W.; Manna, L.; Wang, L.; Alivisatos, A. P. Linearly Polarized Emission from Colloidal Semiconductor Quantum Rods. *Science* **2001**, *292*, 2060–2063.
- (19) Anc, M. J.; Pickett, N. L.; Gresty, N. C.; Harris, J. A.; Mishra, K. C. Progress in Non-Cd Quantum Dot Development for Lighting Applications. ECS J. Solid State Sci. Technol. 2013, 2, R3071—R3082.
- (20) Li, L.; Pandey, A.; Werder, D. J.; Khanal, B. P.; Pietryga, J. M.; Klimov, V. I. Efficient Synthesis of Highly Luminescent Copper Indium Sulfide-Based Core/Shell Nanocrystals with Surprisingly Long-Lived Emission. *J. Am. Chem. Soc.* **2011**, *133*, 1176–1179.
- (21) Pons, T.; Pic, E.; Lequeux, N.; Cassette, E.; Bezdetnaya, L.; Guillemin, F.; Marchal, F.; Dubertret, B. Cadmium-Free CuInS2/ZnS Quantum Dots for Sentinel Lymph Node Imaging with Reduced Toxicity. *ACS Nano* **2010**, *4*, 2531–2538.
- (22) Aldakov, D.; Lefrançois, A.; Reiss, P. Ternary and Quaternary Metal Chalcogenide Nanocrystals: Synthesis, Properties and Applications. *J. Mater. Chem. C* **2013**, *1*, 3756–3776.
- (23) Kolny-Olesiak, J.; Weller, H. Synthesis and Application of Colloidal CuInS2 Semiconductor Nanocrystals. *ACS Appl. Mater. Interfaces* **2013**, *5*, 12221–12237.
- (24) Allen, P. M.; Bawendi, M. G. Ternary I-III-VI Quantum Dots Luminescent in the Red to Near-Infrared. J. Am. Chem. Soc. 2008, 130, 9240-9241.
- (25) van der Stam, W.; Bladt, E.; Rabouw, F. T.; Bals, S.; de Mello Donega, C. Near-Infrared Emitting CuInSe<sub>2</sub>/CuInS<sub>2</sub> Dot Core/Rod Shell Heteronanorods by Sequential Cation Exchange. *ACS Nano* **2015**, *9*, 11430–11438.
- (26) Kruszynska, M.; Borchert, H.; Parisi, J.; Kolny-Olesiak, J. Synthesis and Shape Control of CuInS2 Nanoparticles. *J. Am. Chem. Soc.* **2010**, *132*, 15976–15986.
- (27) Xia, C.; Winckelmans, N.; Prins, P. T.; Bals, S.; Gerritsen, H. C.; de Mello Donegá, C. Near-Infrared-Emitting CuInS 2/ZnS Dotin-Rod Colloidal Heteronanorods by Seeded Growth. *J. Am. Chem. Soc.* **2018**, *140*, 5755–5763.
- (28) Cai, C.; Zhai, L.; Zou, C.; Li, Z.; Zhang, L.; Yang, Y.; Huang, S. Cu1.94S-Assisted Growth of Wurtzite CuInS2 Nanoleaves by In Situ Copper Sulfidation. *Nanoscale Res. Lett.* **2015**, *10*, No. 294.
- (29) Zhao, M.; Huang, F.; Lin, H.; Zhou, J.; Xu, J.; Wu, Q.; Wang, Y. CuGaS2-ZnS p-n Nanoheterostructures: A Promising Visible Light Photo-Catalyst for Water-Splitting Hydrogen Production. *Nanoscale* **2016**, *8*, 16670–16676.
- (30) Adhikari, S. Das; Dutta, A.; Prusty, G.; Sahu, P.; Pradhan, N. Symmetry Break and Seeded 2D Anisotropic Growth in Ternary CuGaS2 Nanocrystals. *Chem. Mater.* **2017**, *29*, 5384–5393.
- (31) van der Stam, W.; Berends, A. C.; Rabouw, F. T.; Willhammar, T.; Ke, X.; Meeldijk, J. D.; Bals, S.; de Mello Donega, C. Luminescent  $CuInS_2$  Quantum Dots by Partial Cation Exchange in  $Cu_{2-x}S$  Nanocrystals. *Chem. Mater.* **2015**, *27*, 621–628.
- (32) Li, J.; Bloemen, M.; Parisi, J.; Kolny-Olesiak, J. Role of Copper Sulfide Seeds in the Growth Process of CuInS2 Nanorods and Networks. ACS Appl. Mater. Interfaces 2014, 6, 20535–20543.
- (33) Pan, D.; An, L.; Sun, Z.; Hou, W.; Yang, Y.; Yang, Z.; Lu, Y. Synthesis of Cu–In–S Ternary Nanocrystals with Tunable Structure and Composition. *J. Am. Chem. Soc.* **2008**, *130*, 5620–5621.

(34) Lu, X.; Zhuang, Z.; Peng, Q.; Li, Y. Controlled Synthesis of Wurtzite CuInS2 Nanocrystals and Their Side-by-Side Nanorod Assemblies. *CrystEngComm* **2011**, *13*, 4039–4045.

- (35) Xiao, N.; Zhu, L.; Wang, K.; Dai, Q.; Wang, Y.; Li, S.; Sui, Y.; Ma, Y.; Liu, J.; Liu, B.; et al. Synthesis and High-Pressure Transformation of Metastable Wurtzite-Structured CuGaS2 Nanocrystals. *Nanoscale* **2012**, *4*, 7443–7447.
- (36) Berestok, T.; Guardia, P.; Estradé, S.; Llorca, J.; Peiró, F.; Cabot, A.; Brock, S. CuGaS2 and CuGaS2–ZnS Porous Layers from Solution-Processed Nanocrystals. *Nanomaterials* **2018**, *8*, No. 220.
- (37) Chang, S. H.; Chiu, B. C.; Gao, T. L.; Jheng, S. Iou; Tuan, H. Y. Selective Synthesis of Copper Gallium Sulfide (CuGaS2) Nanostructures of Different Sizes, Crystal Phases, and Morphologies. CrystEngComm 2014, 16, 3323–3330.
- (38) Regulacio, M. D.; Ye, C.; Lim, S. H.; Zheng, Y.; Xu, Q.-H.; Han, M.-Y. Facile Noninjection Synthesis and Photocatalytic Properties of Wurtzite-Phase CuGaS2 Nanocrystals with Elongated Morphologies. *CrystEngComm* **2013**, *15*, 5214–5217.
- (39) Tung, H.-T.; Hwu, Y.; Chen, I.-G.; Tsai, M.-G.; Song, J.-M.; Kempson, I. M.; Margaritondo, G. Fabrication of Single Crystal CuGaS<sub>2</sub> Nanorods by X-Ray Irradiation. *Chem. Commun.* **2011**, 47, 9152–9154.
- (40) Peng, Z. A.; Peng, X. Nearly Monodisperse and Shape-Controlled CdSe Nanocrystals via Alternative Routes: Nucleation and Growth. *J. Am. Chem. Soc.* **2002**, *124*, 3343–3353.
- (41) Lee, S. M.; Cho, S. N.; Cheon, J. Anisotropic Shape Control of Colloidal Inorganic Nanocrystals. *Adv. Mater.* **2003**, *15*, 441–444.
- (42) Kumar, S.; Nann, T. Shape Control of II-VI Semiconductor Nanomaterials. *Small* **2006**, 2, 316–329.
- (43) Zhai, Y.; Shim, M. Cu<sub>2</sub>S/ZnS Heterostructured Nanorods: Cation Exchange vs Solution-Liquid-Solid-like Growth. *ChemPhysChem* **2016**, *17*, 741–751.
- (44) De Trizio, L.; Prato, M.; Genovese, A.; Casu, A.; Povia, M.; Simonutti, R.; Alcocer, M. J. P.; D'Andrea, C.; Tassone, F.; Manna, L. Strongly Fluorescent Quaternary Cu–In–Zn–S Nanocrystals Prepared from Cu<sub>1-x</sub>InS<sub>2</sub> Nanocrystals by Partial Cation Exchange. *Chem. Mater.* **2012**, *24*, 2400–2406.
- (45) Li, Q.; Zhai, L.; Zou, C.; Huang, X.; Zhang, L.; Yang, Y.; Chen, X.; Huang, S. Wurtzite CuInS2 and  $CuIn_xGa_{1-x}S_2$  Nanoribbons: Synthesis, Optical and Photoelectrical Properties. *Nanoscale* **2013**, *5*, 1638–1648.
- (46) Madelung, O. Semiconductors: Data Handbook, 3rd ed.; Springer: Marburg, Germany, 2004.
- (47) Wang, J. J.; Wang, Y. Q.; Cao, F. F.; Guo, Y. G.; Wan, L. J. Synthesis of Monodispersed Wurtzite Structure CuInSe2 Nanocrystals and Their Application in High-Performance Organic-Inorganic Hybrid Photodetectors. J. Am. Chem. Soc. 2010, 132, 12218–12221.
- (48) Oh, N.; Shim, M. Metal Oleate Induced Etching and Growth of Semiconductor Nanocrystals, Nanorods, and Their Heterostructures. *J. Am. Chem. Soc.* **2016**, *138*, 10444–10451.
- (49) Smith, A. M.; Mohs, A. M.; Nie, S. Tuning the Optical and Electronic Properties of Colloidal Nanocrystals by Lattice Strain. *Nat. Nanotechnol.* **2008**, *4*, No. 56.
- (50) Ryu, E.; Kim, S.; Jang, E.; Jun, S.; Jang, H.; Kim, B.; Kim, S.-W. Step-Wise Synthesis of InP/ZnS Core—Shell Quantum Dots and the Role of Zinc Acetate. *Chem. Mater.* **2009**, *21*, 573—575.
- (51) Zhong, H.; Bai, Z.; Zou, B. Tuning the Luminescence Properties of Colloidal I–III–VI Semiconductor Nanocrystals for Optoelectronics and Biotechnology Applications. *J. Phys. Chem. Lett.* **2012**, *3*, 3167–3175.
- (52) Mao, B.; Chuang, C.-H.; Wang, J.; Burda, C. Synthesis and Photophysical Properties of Ternary I–III–VI AgInS<sub>2</sub> Nanocrystals: Intrinsic versus Surface States. *J. Phys. Chem. C* **2011**, *115*, 8945–8954.
- (53) Kalyuzhny, G.; Murray, R. W. Ligand Effects on Optical Properties of CdSe Nanocrystals. *J. Phys. Chem. B* **2005**, *109*, 7012–7021.
- (54) Fuhr, A. S.; Yun, H. J.; Makarov, N. S.; Li, H.; McDaniel, H.; Klimov, V. I. Light Emission Mechanisms in CuInS2 Quantum Dots

Evaluated by Spectral Electrochemistry. ACS Photonics 2017, 4, 2425–2435.

(55) Rabouw, F. T.; van der Bok, J. C.; Spinicelli, P.; Mahler, B.; Nasilowski, M.; Pedetti, S.; Dubertret, B.; Vanmaekelbergh, D. Temporary Charge Carrier Separation Dominates the Photoluminescence Decay Dynamics of Colloidal CdSe Nanoplatelets. *Nano Lett.* **2016**, *16*, 2047–2053.